JGR Earth Surface

RESEARCH ARTICLE
10.1029/2018JF004776

Constraining Recent Ice Flow History at Korff Ice Rise, West Antarctica, Using Radar and Seismic Measurements of Ice Fabric

A. M. Brisbourne[1], C. Martín[1], A. M. Smith[1], A. F. Baird[2], J. M. Kendall[2], and J. Kingslake[3]

[1]British Antarctic Survey, Natural Environment Research Council, Cambridge, UK, [2]School of Earth Sciences, University of Bristol, Bristol, UK, [3]Lamont-Doherty Earth Observatory, Columbia University, New York, New York, USA

Key Points:
- Backscatter power anomaly and phase difference in polarimetric radar data have been used to constrain ice fabric variation with depth
- Fabric derived from seismic observations is consistent with the fabric derived from radar measurements
- Fabric at Korff Ice Rise indicates a previous episode of grounded north-south ice flow prior to ice divide formation

Correspondence to:
C. Martín,
cama@bas.ac.uk

Citation:
Brisbourne, A. M., Martín, C., Smith, A. M., Baird, A. F., Kendall, J. M., & Kingslake, J. (2019). Constraining recent ice flow history at Korff Ice Rise, West Antarctica, using radar and seismic measurements of ice fabric. *Journal of Geophysical Research: Earth Surface*, *124*, 175–194. https://doi.org/10.1029/2018JF004776

Received 1 JUN 2018
Accepted 20 DEC 2018
Accepted article online 7 JAN 2019
Published online 25 JAN 2019

Abstract The crystal orientation fabric of ice reflects its flow history, information which is required to better constrain projections of future ice sheet behavior. Here we present a novel combination of polarimetric phase-sensitive radar and seismic anisotropy measurements to provide independent and consistent constraints on ice fabric at Korff Ice Rise, within the Weddell Sea sector of West Antarctica. The nature and depth distribution of fabric in the ice column is constrained using the azimuthal variation in (1) the received power anomaly and phase difference of polarimetric vertical radar soundings and (2) seismic velocities and shear wave splitting measurements. Radar and seismic observations are modeled separately to determine the nature and strength of fabric within the ice column. Both methods indicate ice fabric above 200-m depth which is consistent with present-day ice-divide flow. However, both measurements also indicate an oblique girdle fabric below 230-m depth within the ice column, inconsistent with steady state divide flow. Our interpretation is that this deeper fabric is a remnant fabric from a previous episode of flow, which is currently being overwritten by ongoing fabric development associated with the present-day flow regime. The preexisting fabric is consistent with ice flow from the south prior to ice-divide formation, in agreement with models of Holocene ice sheet evolution. These findings apply new constraints to the flow history at Korff Ice Rise prior to divide formation and demonstrate the capacity of radar and seismic measurements to map fabric and thus constrain past ice flow.

Plain Language Summary When ice flows its crystals become oriented in specific ways dependent on the way the ice is flowing, forming what we call a fabric. When this occurs in an ice stream the form of this fabric is determined by the flow direction and geometry of the ice stream bed. These fabrics remain imprinted within the ice but can become overwritten by new fabrics which result from a subsequent flow pattern. The study site here is Korff Ice Rise, which is an isolated area of grounded ice within the floating Ronne Ice Shelf in the Weddell Sea, West Antarctica. Here the ice flows in a very specific way, forming a characteristic fabric. We can measure this fabric using radar and seismic measurements. We also see an older fabric which must have formed when the ice was flowing differently. This older fabric is consistent with a time when the ice sheet was much thinner and ice was flowing from the continent of Antarctica further upstream, and over the current site. This study shows how measurements of fabric within Antarctic ice help us look at how the ice sheet behaved in the past. This past behavior would have affected global sea levels.

1. Introduction

Knowledge of the past behavior of the West Antarctic Ice Sheet is key to evaluating future projections of sea level rise with predictive ice sheet models (e.g., DeConto & Pollard, 2016). Critically, the Weddell Sea region of West Antarctica exhibits some of the largest changes in ice sheet extent since the last glacial maximum (LGM; ~26 to 19 ka B.P. (Bentley et al., 2010; Clark et al., 2009; Hillenbrand et al., 2014; Kingslake et al., 2018)). The configuration of the post-LGM ice sheet has implications for the likely sea level rise contribution of this region. Furthermore, the potential importance of the Weddell Sea region to future sea level rise is emphasized by the presence of a reverse bed slope, which can lead to positive ice loss feedback and rapid retreat (Ross et al., 2012). Reconstructions of ice sheet history are also required to correct satellite gravity measurements of contemporary ice-mass change for the effect of long-term glacial isostatic adjustment

(GIA; Velicogna & Wahr, 2006); the Weddell Sea region is the site of a large discrepancy between GIA models and GPS uplift observations (Whitehouse et al., 2012).

Cosmogenic exposure age dating (Bentley et al., 2010), marine radiocarbon dating (Hillenbrand et al., 2014), ice surface lineations (Siegert et al., 2013), ice cores (Mulvaney et al., 2007), and internal ice sheet structure (Bingham et al., 2015; Kingslake et al., 2016; Siegert et al., 2013; Winter et al., 2015) have all been used to constrain ice sheet advance and retreat since the LGM in the Weddell Sea region. Recent flow reorganization remains poorly constrained (Bentley et al., 2010; Clark et al., 2009; Hillenbrand et al., 2014), and therefore, the contribution to sea level rise since the LGM remains uncertain (Bentley, 1999). Post-LGM retreat of the grounding line to inland of its current position, followed by more recent advance, has been proposed by a number of authors (Bradley et al., 2015; Kingslake et al., 2018; Siegert et al., 2013). This sequence, corroborated by ice sheet modeling (Kingslake et al., 2018), potentially explains the presence of ice streams currently resting on reverse bed slopes along the grounding line of the Weddell Sea, which otherwise raise questions of how the ice sheet retreat could have stabilized in this configuration (Bradley et al., 2015). Together, these studies provide a data set in the Weddell Sea that, although sparse, provides a glimpse of a flow history perhaps more complex than a simple monotonic retreat from LGM to present.

The flow history of ice is preserved in its fabric, which reflects the resultant crystal-orientation fabric (COF): the *c* axes rotate toward the compressive axis (Azuma & Higashi, 1985). In turn, this fabric influences the viscosity of the ice, a result of shear strength parallel to the *c* axis of the hexagonal ice crystals being several orders of magnitude greater than the shear strength perpendicular (Duval et al., 1983). The range of potential fabrics is limited by hexagonal ice and the range of stress regimes present in ice sheets. For example, in the case of a perfect dome, ice deforms by vertical uniaxial compression alone, rotating the *c* axes toward the vertical and resulting in a vertical transverse isotropic (VTI), or cluster, fabric which strengthens with depth due to the increasing compressive strain (Alley, 1988). The *c* axis is rotationally invariant around the vertical axis. Measurement of fabric in thin sections of ice cores from ice domes consistent with this model have been reported (Azuma et al., 1999; Durand et al., 2007; Montagnat et al., 2012; Thorsteinsson et al., 1997; Wang et al., 2003; Weikusat et al., 2017). At ice divides, where a lateral component of tension is present, a vertical girdle fabric (also known as Horizontal Transverse Isotropy) develops, where the *c* axes lie in a diffuse girdle orthogonal to the direction of extension (Bargmann et al., 2012; Faria et al., 2014; Lipenkov et al., 1989; Wang et al., 2002; Weikusat et al., 2017). Deviations from this simple fabric configuration are attributed to dynamic recrystallization processes (Diprinzio et al., 2005; Thorsteinsson et al., 1997) or ice viscosity variation (Durand et al., 2007). Martin et al. (2009) demonstrate that ice-divide fabrics require at least 4 times the characteristic time to develop, where the characteristic time is the ratio of ice thickness to accumulation rate. The englacial structure of an ice divide takes up to 10 times the characteristic time to reach steady state. The englacial structure and fabric therefore potentially provide constraints on the timing of processes.

The use of geophysical methods to measure COF variation in ice has been verified by agreement with ice core thin section data using radar (Drews et al., 2012; Eisen et al., 2007; Fujita et al., 2006; Matsuoka et al., 2003, 2009), sonic logging (Gusmeroli et al., 2012), and combined radar and seismic measurements (Diez et al., 2015). Away from ice rises, both passive and active-source seismic data have been used to constrain fabric. For example, Picotti et al. (2015) used controlled source seismic data to constrain COF at Whillans Ice Stream, where a fabric consistent with basal sliding and bed deformation is measured. Smith et al. (2017) used icequakes from the bed to constrain a more complex fabric at Rutford Ice Stream, resulting from laterally constricted ice stream flow.

In this study we combine polarimetric phase-sensitive radar (ApRES) and controlled-source seismic measurements to determine the fabric in the ice column at Korff Ice Rise (KIR). The azimuthal variation in radar return power and phase is modeled to determine COF variation with depth. Similarly, azimuthal variation in seismic velocities and shear wave splitting observations provide diagnostic observations which are modeled using seismic ray-tracing to test possible configurations of fabric. By assuming that fabric which is inconsistent with present-day flow reflects previous ice flow episodes, fabric is used to infer the recent ice flow history at KIR, providing new constraints on deglaciation in the Weddell Sea region in an area with limited observations. We discuss the implications of these new flow regimes and the limitations of our methods, outlining improvements for future studies.

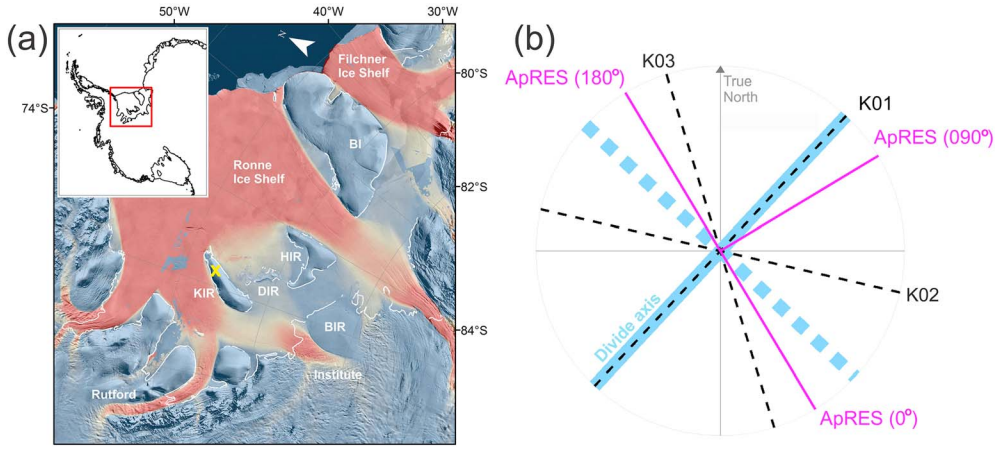

Figure 1. Field site and experimental setup. (a) The Weddell Sea and Filchner-Ronne ice shelf area with inset showing location within West Antarctica. Korff Ice Rise (KIR), Henry Ice Rise (HIR), Bungenstock Ice Rise (BIR), Doake ice rumples (DIR), Berkner Island (BI), and the institute and Rutford ice streams are labeled. Satellite-derived ice flow velocities (color map), ice flow direction (scaled red arrows), and grounding line (white; Rignot et al., 2011a) are overlain on the MODIS imagery (Scambos et al., 2007). The radar and seismic experiments were carried out 700 m apart at the northern end of KIR (yellow cross). (b) Acquisition geometry relative to the ice divide axis. Orientation of the Korff Ice Rise divide axis (blue solid) and its perpendicular (blue dash). Seismic line K01 is along the divide axis with K02 and K03 at 60° rotation. The ApRES cross sections are oriented almost perpendicular to the divide (16° west) and rotation was counterclockwise from 0° to 180°.

2. The Study Site

KIR is an area of grounded slow-moving ice within the Ronne Ice Shelf, West Antarctica (Figure 1a). Ice thickness at the northern end of KIR is around 500 m and ice is grounded approximately 250 m below sea level. Ice flow at the divide is currently perpendicular to the ridge axis at surface rates of <10 m/a. The present-day ice divide is orientated along 043° (Figure 1a). The surrounding ice currently flows from the Institute and Rutford Ice Streams to the south. This floating shelf-ice flows northward, parallel to the length of KIR, with velocities of over 300 m/a to the west of KIR and around 150 m/a to the east over the Doake Ice Rumples (Rignot et al., 2011a).

Kingslake et al. (2016) used a technique termed Raymond Effect Dating (RED; Raymond, 1983), which utilizes the distinctive englacial structure of ice divides that results from nonlinear ice-flow behavior, to constrain flow history at KIR (Conway et al., 1999; Martin et al., 2009). They combined inversion for two-dimensional flow with both radar observations of englacial structures and present-day flow rates to date the formation age of the current englacial structure. Their results indicate that KIR is currently not in steady state, and imply that a regional flow reorganization occurred at around 2.5 ka B.P. Although the preceding flow direction could not be constrained, they infer that the ice was slow moving and grounded, prior to the current phase of divide flow.

3. The Effects of Anisotropic Media on the Propagation of Radar and Seismic Waves

3.1. Representation of COF in Ice

The widely used nomenclature of COF in ice, such as cluster or girdle fabric, relates to the geometry of the envelopes which encapsulate the *c* axes of the fabric (e.g., Diez & Eisen, 2015). In a VTI, or cluster, fabric the *c* axes are orientated in vertical cone shapes. In a vertical girdle fabric the *c* axes are oriented in a girdle around a vertical plane. The normal to this plane is the horizontal symmetry axis. In a laterally unconstrained flow regime a girdle fabric geometry will form with the symmetry axis parallel to the flow or extension direction. For consistency, in this manuscript we refer to the orientation of a girdle fabric by the orientation of the symmetry axis, the normal to the girdle plane.

Fabric strength may be described by the relative tightness of the cluster or girdle and quantified by the opening angle of the envelope (Diez & Eisen, 2015). The strength of the fabric may also be described by the eigenvalues of an ellipsoid fit to the envelope geometry (Diez & Eisen, 2015). Another common way of representing a fabric geometry and its strength is hemispherical projections of the *c* axes (Walker & Wookey, 2012), or a Schmidt plot, whereby the density of projections of the *c* axes onto a hemisphere form a graphical representation of the fabric geometry and strength.

3.2. ApRES

Ice-penetrating radar returns, or reflections, result from backscatter at contrasts in dielectric properties at depth in the ice column. Changes in density, acidity, and fabric all potentially result in dielectric property contrasts. In an anisotropic medium the two mechanisms that affect the polarization and azimuthal variation in power of radar returns are birefringence and anisotropic scattering. In birefringent ice an electromagnetic wave becomes resolved into two components, or orthogonal waves, oriented along the directions of the allowed electric vectors in the medium (Hargreaves, 1977). The orientation of these vectors is controlled by the relative orientation of the propagation direction to the *c* axes. Initially, the components are in phase, but differences in dielectric permittivity along the two planes control the relative speed of propagation, and produce a phase shift between the waves. The phase shift results in interference between the waves when observed at the receiving antenna and produces characteristic variation with azimuth in power and phase, known as birefringence. Birefringence is therefore a consequence of a bulk crystal-preferred orientation fabric which is azimuthally asymmetric with respect to the propagation direction (e.g., Drews et al., 2012), as radio waves travel at different speeds on different longitudinal planes. In contrast, anisotropic scattering is a consequence of rapid but microscopic continuous depth variations in the orientation of the bulk crystal-preferred orientation fabric, a result of initial heterogeneity from the original year-to-year depositional layer structure variability (e.g., Eisen et al., 2007). Thus, anisotropic scattering typically occurs with some degree of birefringence. However, one form may dominate any received signal and obscure the other. Changes with depth in the overall anisotropic scattering signal result from variation in the orientation of the bulk fabric upon which the scattering is superimposed (Fujita et al., 2006) and are possibly a result of variations in strain of initially heterogeneous ice layering at the larger scale due to, for example, climatic variation (Drews et al., 2012).Polarimetric radar measurements used here utilize a linearly polarized source and receiver with a normal-incidence fixed offset geometry. Both source and receiver are rotated relative to the medium and subsequently reconciled to reconstruct the azimuthal variations in power and phase. For each orientation, the two orthogonal waves described above are observed at a polarized receiver as a single waveform formed by the interference of the two waves; the observed waveform is controlled by the interference resulting from the phase difference between the two waves and also the relative orientation of the receiver. Rotation of the source and receiver allows the determination of the variation in return power and phase with azimuth, which is controlled by the variation with azimuth of the interference of the two orthogonal waves. The variation in return power and phase with azimuth allows the discrimination of fabric.

3.3. Seismics

Seismic energy also undergoes scattering during propagation due to heterogeneity in the media. However, seismic observations are generally considered in terms of reflections which are coherent returns which result from contrasts in the elastic moduli and density at an interface, that is, the acoustic impedance contrast. Seismic observations of fabric measure the bulk effect over the propagation path in terms of azimuthal and offset dependence of seismic velocity or birefringence, for example. In a similar way to electromagnetic energy, a seismic shear wave incident at an anisotropic medium may split into two orthogonal waves which travel at different speeds determined by the differences in elastic moduli resulting from the fabric and its orientation. The split waves interfere with one another in a way that depends on the strength and orientation of the fabric, the path length, and the source-receiver azimuths and configuration. Seismic methods record the full wavefield using three-component receivers at a range of offsets and azimuths. The split shear waves are observed on the three orthogonal components of the receiver, with each recorded waveform determined by the relative orientation of the receiver component to the polarity of the incoming shear waves and the time lag, or phase difference, between the shear waves. These measurements are analyzed to determine relative velocities and fabric symmetry using relative travel times and polarization directions. In seismic data, azimuthal variation in velocity, phase, and amplitude are all diagnostic of fabric.

Although the radar and seismic methods are sensitive to different physical parameters of ice, dielectric permittivity, and elastic moduli, respectively, equivalent measurements can be made which are diagnostic of the crystal orientation fabric. The respective analysis methods differ between the two measurements due to fundamental differences in acquisition methods. Also, the acquisition geometry used results in radar measurements which are restricted to the vertical axis, whereas the seismic measurements sample a range of propagation angles within the ice column. This enhances the capability of the seismic method allowing the discrimination of different fabric types. In addition, azimuthal variations in *P* wave (longitudinal) seismic wave velocities allow additional constraints to be placed on the fabric geometry. There is no equivalent measurement using radar.

4. Data Acquisition

4.1. Polarimetric Phase-Sensitive Radar

Polarimetric measurements were acquired using a phase-sensitive frequency modulated continuous-wave radar (ApRES; Nicholls et al. (2015)) at the ice divide of northern KIR in December 2014 (W068.431°, S78.720°). The ice thickness at the ApRES site is 558 ± 5 m. The system was configured to transmit chirps that varied linearly between 200 and 400 MHz in time intervals of 1 s. We followed Hargreaves (1977) and Fujita et al. (2006) and implemented a co-parallel experiment with transmitting and receiving antennas deployed parallel and 7 m apart. The englacial optical anisotropy is derived from differences in power and phase of the return signal as the antenna pair is rotated simultaneously through 15° intervals counterclockwise from 0 to 180° (0° in the experiment frame of reference is 149° true bearing, or 16° east of the perpendicular to the divide axis (Figure 1b)). In these co-parallel measurements, the azimuthal variations in the return signal are a consequence of azimuthal variations in crystal-preferred orientation fabrics and are insensitive to fabrics that do not display azimuthal variation around the vertical axis, such as a vertical cluster.

4.2. Seismic Reflection Gathers

In January 2015, three wide-angle common midpoint seismic reflection gathers were acquired, centered on the ice divide at the northern end of Korff Ice Rise (W068.414°, S78.714°), approximately 700 m north along the ridge axis from the ApRES measurements. The ice thickness at the seismic site is 530 ± 5 m, as determined by radar profile data (Kingslake et al., 2016). The three gathers were oriented at 60° to one another to constrain azimuthal variation in seismic properties (Figure 1b). Each gather used four shot points, each with 48 receivers at 10-m intervals. The offset to the first receiver ranged from 30 to 1,440 m, producing traces out to 1,940-m offset, or incidence angle at the bed up to 58°. To achieve three-component recordings, the receivers were oriented to measure either vertical, radial, or transverse motion. The common midpoint gather along the divide axis (K01; true bearing 043°) was shot twice: once with all sensors orientated vertically using 150 g of high explosive and once with horizontal sensors alternating radial and transverse orientation, using 600-g shots; the latter resulting in an effective 20-m receiver interval for the horizontal components. The oblique common midpoint gathers (K02: 60° east of K01; K03: 60° west of K01) were shot once only, each with 600-g shots and alternating vertical, radial, and transverse receivers, resulting in an effective 30-m receiver interval for all three components. The larger shot is required to generate sufficient *S* wave energy at the source. Although an explosive source in a homogeneous isotropic medium will theoretically not generate *S* wave energy, the nonuniform nature of the shallow firn results in significant *S* wave energy (for discussion, see King & Jarvis (2007)). The acquisition geometry results in a midpoint basal reflection ellipse with a length of 235 m. The Fresnel zone is less than 80 m (minimum 150-Hz dominant frequency). Data were recorded on a 48-channel system with 2-s record length at 8,000-Hz sample rate with 40-Hz receivers. Shot and receiver elevation statics were applied although the surface elevation varies by less than 10 m across the survey area.

5. Analytical Methods

Due to the nature of the measurements, sensitivity to different parameters, and differing assumptions required, radar and seismic data are processed and modeled separately and reconciled at a later stage to establish the consistency and equivalence of the two independent methods. We model a suite of observations to constrain the basal properties and ice fabric present in the ice column. Fabric models, derived from the

likely historic flow regimes present in the region, are then tested to determine the configuration which best satisfies these key observations.

5.1. ApRES

5.1.1. Data Processing

By collecting co-parallel radar measurements through orientations of 0 to 180° we are able to reconstruct the full azimuthal range of return power anomaly and phase difference. The anomaly of radar return power is derived by removing, for a given depth, the mean of the return power across all 13 measured orientations, eliminating the mechanisms that are independent of azimuth. Similarly, we calculate the azimuthal variation in the phase of returns by subtracting, for a given depth, the phase of the signal between contiguous measurement azimuths; that is, at say 500-m depth we calculate the difference between the phase measured at 0 and 15°, then 15 and 30°, then 30 and 45°, and so on to produce an azimuthal variation in phase at 500-m depth.

5.1.2. Modeling ApRES Data and Data Analysis

We use the matrix-based method of Fujita et al. (2006) to model the azimuthal variation in power anomaly and phase difference, that is, the variation which would result from the change in interference between the orthogonal electromagnetic waves as recorded by a rotating polarized source-receiver pair. This model utilizes the difference in permittivity along the principal horizontal axes, from which we derive the eigenvalues of the orientation tensor by assuming a vertical girdle fabric. When flow-induced, the symmetry axis of this girdle fabric indicates the direction of flow extension (Azuma, 1994). As stated previously, the ApRES measurements are insensitive to any azimuthally symmetric fabric.

As suggested by Fujita et al. (2006), an effective way of estimating the fabric strength is analyzing the depth dependence of the azimuthal variation in the backscatter power anomaly. We have extended this analysis to also include the phase difference. By way of illustration we present synthetic power anomaly and phase difference plots for a one-layer model formed of a perfect girdle fabric (opening angle of 0°, i.e., all *c* axes in a vertical plane) with the symmetry axis at 90°. For a model of birefringent ice without anisotropic scattering boundaries (Figure 2a), a 90° symmetry in the power anomaly is observed with pairs of "nodes," or minima in the power anomaly, at 90° to one another and recurring with depth. The locations of the nodes in the power anomaly are coincident with rapid phase-difference sign reversals with depth. For a model of anisotropic scattering with no birefringence (Figure 2b), the power anomaly displays a 180° periodicity but no variation in phase difference. For a model combining both birefringent ice and anisotropic scattering (Figure 2c), the scattering signal dominates the power anomaly, with 180° periodicity but some modification by the birefringence signal resulting in relatively weak nodes separated by <90°. The phase anomaly signal for the combined model is dominated by the birefringent signal with characteristic "four-quadrant patterns" formed by the azimuthal rotation of the phase-difference sign reversals. In this combined model the center of the quadrant pattern aligns with the symmetry axis. The nodes and quadrant patterns occur at the same depths in the combined model as in the birefringence-only model.

The features termed nodes result from a minimum in backscattered power which occurs every time the difference in phase between the fast and slow waves is a multiple of π, when minima in waveforms coincide. The orientation of the nodes gives an indication of the azimuth of the symmetry axis. The separation in time between nodes, or difference in depth, gives an indication of the difference in permittivity between the fast and slow axes. The nodes will be more closely spaced in depth if the azimuthal difference in permittivity, or fabric strength, is greater. A similar mechanism and interpretation of the phase-difference sign reversals is also valid, and it should be noted that where nodes in the power anomaly are weak due to strong anisotropic scattering, phase-difference sign reversals or the characteristic quadrant patterns remain diagnostic.

5.2. Seismic Data Analysis

The seismic acquisition captured a range of phases including direct *P* and *S* reflections, *P* to *S* ice-base conversions, surface-multiple reflections, surface waves, and diving waves, all at three different azimuths and over a range of bed incidence angles from 0 to 58° (Figure 3). From these comprehensive measurements we use *P* and *S* wave diving waves in the first ice layer and shear wave splitting of *S* wave reflections from the bed to constrain the ice fabric.

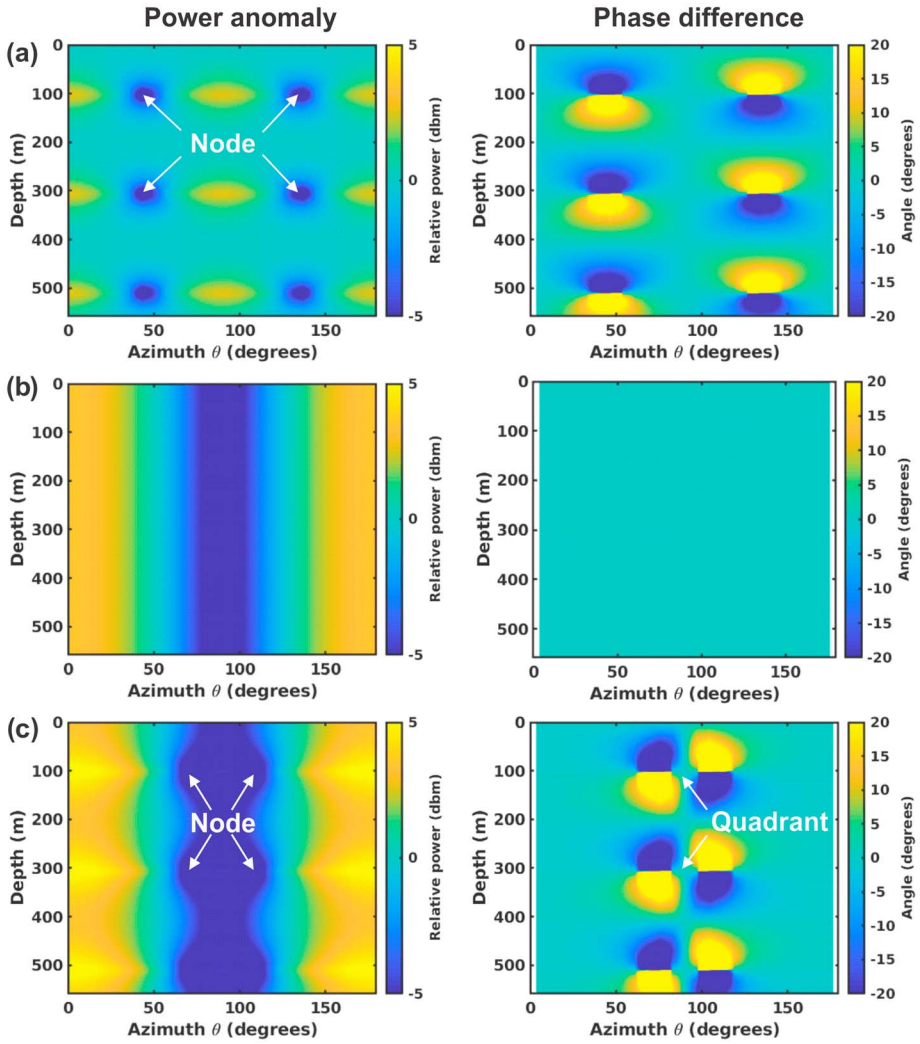

Figure 2. Modeled phase-sensitive radar return power anomaly (left-hand column) and phase difference (right-hand column) as a function of depth and azimuth. The model is formed of a single layer of perfect girdle fabric (opening angle of 0°, i.e., all *c* axes in a vertical plane) with the symmetry axis at 90°. (a) Birefringent ice without anisotropic scattering boundaries, (b) anisotropic scattering but no birefringence, and (c) birefringent ice with anisotropic scattering. Minima in the backscattered power form "nodes" in the power anomaly with coincident phase-difference sign reversals. In media with both birefringence and anisotropic scattering the phase-difference sign reversals can rotate to form characteristic "four-quadrant patterns."

5.2.1. Travel Time Inversion

The compaction of surface snow with increased burial results in rapidly increasing seismic velocity with depth in the firn column. As a result, the seismic raypaths rapidly deviate away from the vertical with increasing depth through the firn layer and arrivals at closely spaced receivers may have traveled significantly different raypaths, which may affect relative amplitude. The velocity-depth profile of the firn layer is determined from seismic *P* wave refraction measurements along line K01 only, using a Wiechert-Herglotz inversion (Kirchner & Bentley, 1990). We assign the firn layer to the depth where the seismic velocity no longer increases. No data were available to measure anisotropy in the firn layer, and it is therefore assumed to be isotropic (Picotti et al., 2015). Similarly, no data were available to determine the *S* wave velocity in the firn and a constant V_p/V_s ratio of 2 (King & Jarvis, 2007).

Beneath the firn layer, the diving waves critically refract along the upper ice layer. Far-offset observations of the diving waves allow direct measurement of the seismic velocity in the upper ice layer. We use the direct *P* and *S* wave arrival times at far offsets across all three azimuths (K01, K02, and K03), picked on the vertical

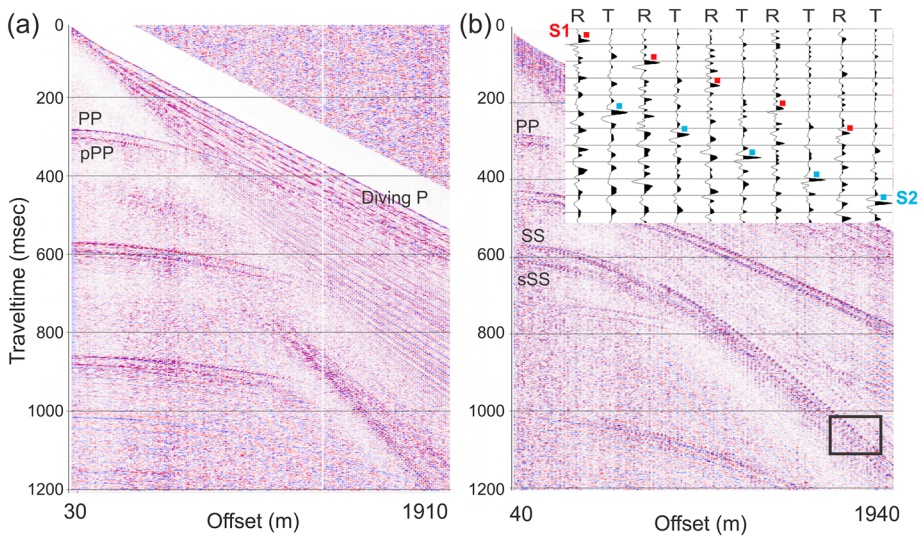

Figure 3. Wide-angle seismic shot gathers from line K02 oblique to the ice divide (with automatic gain control for display purposes only). Gathers are formed from four separate shots at increasing offset, centered at the ice divide. (a) Vertical geophone recording showing clear *P* wave reflections (PP) and two surface multiples. Each reflection is followed by the surface ghost reflection at 20 ms (e.g., pPP). Phases are identified as uppercase for primary paths with ghost paths (shot at 20-m depth reflected from the firn surface) labeled in lowercase. (b) Alternate horizontal radial and transverse recording with an inset highlighting the SS reflection showing shear wave splitting and polarization. Any *S* wave which originates at the source is followed by the surface ghost reflection at ~40 ms (e.g., sSS). The inset to (b) presents fast and slow *S* wave reflection (SS) at far offsets (highlighted by the black box) on the radial (R – red dot) and transverse (T – blue dot) components, respectively. Inset time interval markers are 20 ms.

and radial components, respectively, to quantify the azimuthal velocity variation at the top of the ice column. Direct *P* and *S* wave travel times were measured from the first energy arrivals at offsets beyond 1,000 m where a linear fit can be applied to travel time-offset measurements. The slope of this line is used to derive the *P* and *S* wave velocity at this depth across all three azimuths.

5.2.2. Shear Wave Splitting Analysis

When an *S* wave propagates through anisotropic media it splits into two orthogonal *S* waves, "S1" and "S2." This is known as shear wave splitting or seismic birefringence. As the two independent *S* waves propagate at different velocities they arrive at the receivers separated by a delay time and with polarization controlled by the direction of propagation with respect to the symmetry axis of the fabric (Savage, 1999). Measurements of the delay time and polarization of the fastest *S* wave can be used to constrain the strength and nature of the anisotropic medium.

As described, due to restrictions during acquisition the radial and transverse components are not collocated but separated inline by 10 m. In order to perform standard shear wave splitting analysis to determine delay time and polarization, such as Silver and Chan (1991), we apply a correction to the travel time of the transverse component energy to correct for this offset. A time shift is calculated as a fraction of the delay determined by cross correlation of consecutive radial-component arrivals. This method was tested with synthetic seismograms, demonstrating that the true shear wave splitting measurement can be recovered with standard shear wave splitting techniques (Teanby et al., 2004) after application of a time shift. However, tests showed that the offset-corrected signals frequently cause cycle-skipping errors which makes automated shear wave splitting analysis unreliable. We therefore manually determined the delay time between fast and slow *S* waves at far offsets, where splitting is at its maximum and phase identification is unambiguous. Cycle skipping also precludes the reliable determination of the polarization of the fastest *S* wave as a 90° ambiguity in the polarization is introduced. Although a clear *P*-to-*S* wave conversion (PS) at the bed is observed (Figure 3b), raypath geometry and bed topography preclude its analysis to improve model constraints.

5.2.3. Seismic Ray Tracing in Anisotropic Ice

Elasticity tensors derived from Maurel et al. (2015) are used to produce depth-varying anisotropic models of COF. The tensors are rotated to emulate a range of likely fabric conditions in the ice column. An isotropic

firn layer is assumed, with a velocity gradient determined by the inversion of seismic refraction observations (Kirchner & Bentley, 1990). The strong velocity gradient in the firn affects the raypath geometry and is therefore included in the ray tracing. Velocities within the ice column below the firn are scaled to ensure that the measured normal-incidence travel times match the synthetic travel times assuming an ice column thickness of 530 m, as determined by the radar measurements. Where a layer formed of more than one fabric type is tested, a Voigt-Reuss-Hill average is used (Hill, 1952), a measure of the mean of the upper (Voigt) and lower (Reuss) bounds to the value of the elastic properties of the aggregate. For basal reflections, the software package ATRAK (Guest & Kendall, 1993), based on asymptotic ray theory, is then used to determine travel times and polarities of fast and slow *S* wave reflections. The difference in arrival time is then compared to the observed delay times described above. We do not include conversions and reflections from interfaces within the ice column in our modeling results. This assumption is valid for a number of reasons: (1) no strong seismic reflections are observed from within the ice column and (2) only very weak conversions are expected from likely ice COF interfaces (Diez & Eisen, 2015).

6. Results

A number of qualitative observations indicate the presence of fabric within the ice column: azimuthal variation in radar return power and phase difference, misfit between isotropic synthetic seismic travel times and observations at long offsets (i.e., nonhyperbolic moveout (Baan & Kendall, 2002)), significant energy on the transverse component of the converted *P* to *S* phase, a delayed arrival on the transverse component of the *S* phase, and azimuthal variation in travel times of both direct and reflected seismic energy. However, measurement uncertainties, complex bed topography, and near-surface effects may explain features such as travel time moveout misfit with offset, or *P* to *S* conversion energy on the transverse component. We therefore use only unambiguous measurements, with comparison to synthetic data, to constrain the strength and orientation of fabric within the ice column.

6.1. Phase-Sensitive Radar Measurements

The variation with depth and azimuth of the radar return power anomaly in the co-parallel polarimetric experiment is presented in Figure 4a. Variations in return signal phase difference with azimuth are presented in Figure 4b. If ice were isotropic we would observe no variations in power anomaly or phase difference with azimuth. However, azimuthal variations in power larger than 10 dB are present in the observed backscattered power (Figure 4a). The variation in power anomaly and phase difference in the upper 20 m is attributed to radiation pattern effects. The upper 20–150 m displays no discernible variation in the power anomaly, indicating that the fabric is weak or masked by the radiation pattern. From 150 to 200 m the power anomaly has a periodicity of 180°, indicating that the prevalent mechanism is anisotropic scattering (Figure 2b), a result of rapid variations with depth of ice fabric. Any birefringent effect on return power in our data set is masked by the dominant anisotropic scattering. A transition in both power anomaly and phase difference is observed at 200–230-m depth. Above 200 m we observe minima in return power difference at 015° ± 8°, in our experiment frame of reference (Figure 4a). Beneath 230 m the minima in return power difference are at 110° ± 8°. There is no obvious signature from fabric within the transition depth range at 200–230 m.

For co-parallel measurements as presented here, birefringence, which results from bulk fabric, produces a 90° periodicity with azimuth in the return power anomaly (Figure 2a), whereas anisotropic scattering, resulting from changes in fabric with depth, produces a 180° periodicity (Figure 2b), as seen at 150–200 and below 230 m in Figure 4a. The orientation of the minima in the power anomaly is used to infer the orientation of the symmetry axis (Figure 4a). A more complex relationship is observed in the phase difference (Figure 4b), making variation with depth and azimuth of phase difference diagnostic of both fabric orientation and strength, especially when the power anomaly signal from scattering anisotropy dominates and masks the signal resulting from birefringence.Following the matrix-based method of Fujita et al. (2006), we explored a range of fabric models to determine the configuration which fits the ApRES data. In Figures 4c and 4d we show the synthetic power anomaly and phase difference of this model. We model a vertical girdle fabric with the symmetry axes aligned with 015° above 200 m and 110° below 230 m. The eigenvalue difference of the orientation tensor in the horizontal plane is 0.2 above 200 m and 0.15 below 230 m with scattering 10 dB stronger in the minima than in the maxima direction. We assume that the

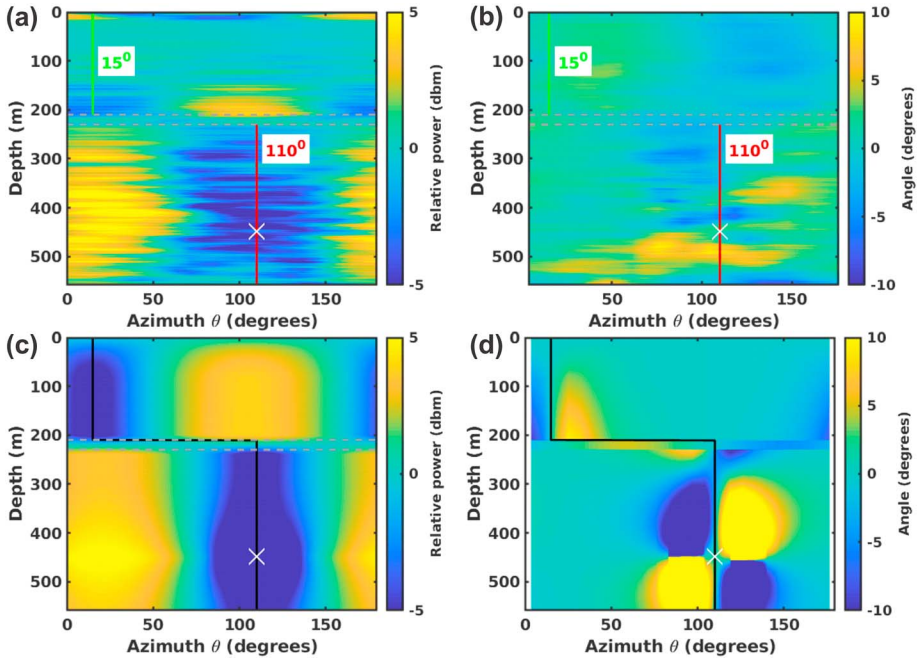

Figure 4. Phase-sensitive radar observations and modeled signal as a function of depth and azimuth in the experiment frame of reference. (a) Return power anomaly and (b) phase difference. The present-day divide axis orientation is 105° in the ApRES experiment frame of reference. A transition from 200 to 230 m is observed in the return power anomaly and bound by dashed lines on all plots. (c) Modeled return power anomaly and (d) modeled phase difference. The model consists of a vertical girdle fabric above and below the transition with the lower girdle rotated 95° relative to the upper girdle. The transition is included in the model as a 30-m-thick layer with no anisotropic scattering. The symmetry axes of the inferred upper (green line) and lower (red line) fabrics at 015 and 110° are highlighted in the data plots. These orientations are used to define the orientation of the girdles in the model and are highlighted in black. The center of the quadrant pattern in the phase difference is highlighted with a white cross.

signal from fabric observed at 150–200 m is masked at shallower depths by the radiation pattern and assign a single fabric to the upper ice layer from 80–200 m. The synthetic results indicate that with such strong anisotropic scattering, nodes due to birefringence would not be visible in the return power anomaly below 230 m (Figure 4c) but quadrant patterns would be visible in the phase difference signal (Figure 4d). This result is consistent with the observations (Figures 4a and 4b), where below the 230-m transition a 180° azimuthal variation dominates the power anomaly but a quadrant pattern is present in the phase difference aligned with 110 ± 8° in the experiment frame of reference (039° true bearing). That is, we can infer that a girdle fabric is present below the 230-m transition with the symmetry axis approximately perpendicular to the girdle fabric determined in the overlying layer.

We cannot however conclude unambiguously that the direction of the minima in power anomaly below the 230-m transition corresponds to the direction of the symmetry axis. It is conceivable that the variations in fabric are perpendicular to the direction of flow, an argument of Drews et al. (2012) for polarimetric radar data near the EPICA ice core site in Dronning Maud Land. However, in addition to the power anomaly the phase change with azimuth indicates that the minima in power anomaly below 230 m (039° true bearing) correspond to the direction of the symmetry axis.

6.2. Seismic Measurements

6.2.1. Diving Wave Travel Times

The Weichert-Herglotz inversion of diving wave travel times indicates a steep seismic velocity gradient in the upper 80 m consistent with rapid densification with depth of the firn. Using this method the seismic *P* wave velocity was determined for a layer of thickness 80 m. This layer is used as the firn layer in subsequent models, 80 m being the depth where the *P* wave velocity ceases to vary with increasing depth.

Table 1
Direct P and S Wave Velocities at the Base of the Firn Column and Uncertainties Derived From Travel Times of Diving Waves

	V_p (m/s)	V_s (m/s)
K01	3814 ± 2	1905 ± 1
K02	3796 ± 3	1924 ± 1
K03	3792 ± 3	1928 ± 1

The first arrivals at far offsets represent energy refracted within the uppermost ice beneath the firn. Using linear regression and accounting for uncertainties in offset and travel time (York et al., 2004), *P* and *S* wave velocities of waves traveling horizontally at the base of the firn were determined for each azimuth. The direct arrival *P* wave velocities are ~0.5% higher along the axis of the divide compared to oblique to it (Table 1). These azimuthally varying *P* wave velocities and V_p/V_s velocity ratios can be modeled with a girdle fabric with symmetry axis perpendicular to the ice divide axis (symmetry axis to 133° ± 12°) with a girdle opening angle of 38° (Figure 5a). The *S* wave travel time picks present the reverse relationship, with V_s along the divide ~1% lower than oblique to it (Table 1). This is the opposite relationship to that expected from the azimuthal variation in *S* wave velocities for a girdle fabric (Figures 5b–5d). These observations are consistent with the S2 phase rather than S1 as the fast *S* wave polarization is consistently radial in the best fit model (Figure 5b), and this is the receiver orientation where all the energy is observed. This points to a more complex fabric than a simple vertical girdle. For example, changes as low as 3° in the opening angle of the girdle fabric would rotate the polarization directions of the S1 phase by 90° along the oblique azimuths of the experiment. Similarly, the addition of 10% cluster fabric rotates the S1 polarization at oblique azimuths. Thin layering in the firn can cause an effective VTI anisotropy (Diez et al., 2016). As such, the presence of a cluster (VTI) fabric in the near surface may add complexity to the media which we are otherwise unable to constrain here.

6.2.2. Shear Wave Splitting

At offsets beyond 1,330 m the fast and slow *S* wave reflection arrival times were picked on the horizontal components (Figure 3b). At shorter offsets the *S* wave reflection amplitudes are weak, or arriving coincident with other phases, impeding unambiguous phase identification. At these far offsets there is no trend in the splitting measurements with respect to offset and a mean value is therefore calculated (Table 2). There is a

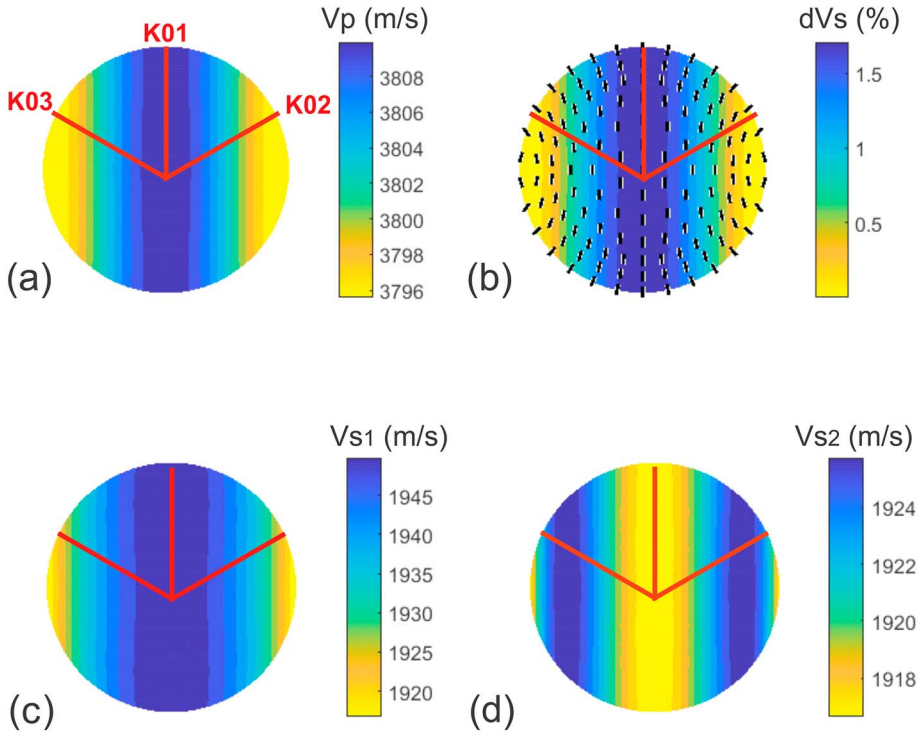

Figure 5. Lower hemisphere plots of seismic properties in a girdle fabric providing the best fit to *P* and *S* diving waves in the uppermost ice at the base of the firn column. The relative orientations of the three seismic gathers are marked in red and labeled. (a) *P* wave velocity (m/s), (b) fast *S* wave polarization direction (black dashes) and percentage of shear wave splitting (color map), (c) fast *S* wave velocity (m/s), and (d) slow *S* wave velocity (m/s). Results are plotted using the MSAT routine of Walker and Wookey (2012).

Table 2
S Wave Splitting Observations (with 2 Standard Deviation Uncertainty) and Synthetic S wave Splitting Measurements for the Three COF Models Tested

	Observations (ms)	Isotropic (ms)	Steady State (ms)	Rotated Girdle (ms)
K01	38.3 ± 2.6	0.0	41.8	37.3
K02	35.8 ± 2.4	0.0	31.5	34.3
K03	19.1 ± 5.8	0.0	31.5	20.6
Mean misfit		30.9	6.7	1.3

Note: Mean uncertainty of the observations is 3.6 ms (2 standard deviations).

clear azimuthal variation in the degree of shear wave splitting, with the greatest degree of splitting measured along K01 and K02, parallel to and 60° east of the divide, respectively. This is twice the splitting measured along K03, which is oriented 60° west of the divide.

The seismic observations are tested against models of ice fabric, informed by the radar observations. The shear wave splitting observations record the integrated effect of the fabric within the entire ice column and cannot be used to delineate the vertical distribution of the fabric. Diving waves provide sampling over specific depths. We therefore use the ApRES observations to constrain a transition in fabric at a depth of 230 m (we use the lower boundary of the transition to define the three-layer model geometry) but constrain the form of the fabric using the seismic observations independently.

A three-layer model, firn over two ice layers (Figure 6), was used to test a range of hypotheses regarding the ice flow history of the region. In all models, an isotropic firn layer is assigned to a depth of 80 m, based on the velocity structure determined by seismic refraction measurements. The firn layer is underlain by the upper ice layer, to a depth of 230 m, to satisfy the ApRES observation of a transition in fabric at this depth. We assign likely COF to the two ice layers based on the fabric expected in steady state flow at ice divides (Martin et al., 2009). Except in the isotropic model, a moderate girdle fabric with the symmetry axis perpendicular to the divide is assigned to the upper ice layer to satisfy the direct *P* and *S* wave velocity measurements, assuming a strengthening of the girdle fabric with depth (Martin et al., 2009). The lower ice layer, from 230 m to the ice base at 530 m, is assigned a range of COF to test possible models. The models tested are (1) isotropic; (2) steady state ice divide with a vertical cluster at depth, as expected at an ice divide which has remained stable for >10 kyr (Martin et al., 2009); and (3) a rotated girdle with a cluster fabric. In this

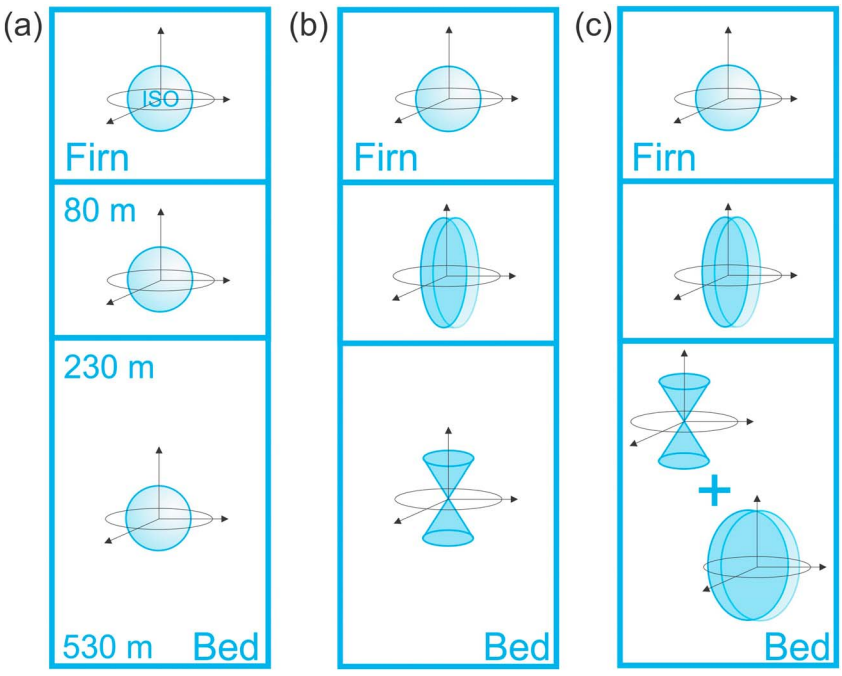

Figure 6. COF models tested represented by sketches of the envelope of the *c* axis distribution. Isotropic firn to 80-m depth based on the velocity structure determined by seismic refraction measurements; then (a) isotropic, (b) a model of a girdle fabric in the upper ice layer over a cluster fabric in the deep ice layer—termed the "steady state" model and representative of ice divide fabric formation alone, and (c) a girdle fabric in the upper ice layer over a cluster fabric in the lower ice layer with a rotated-girdle component in the deeper ice layer representative of preexisting fabric formed prior to ice divide formation.

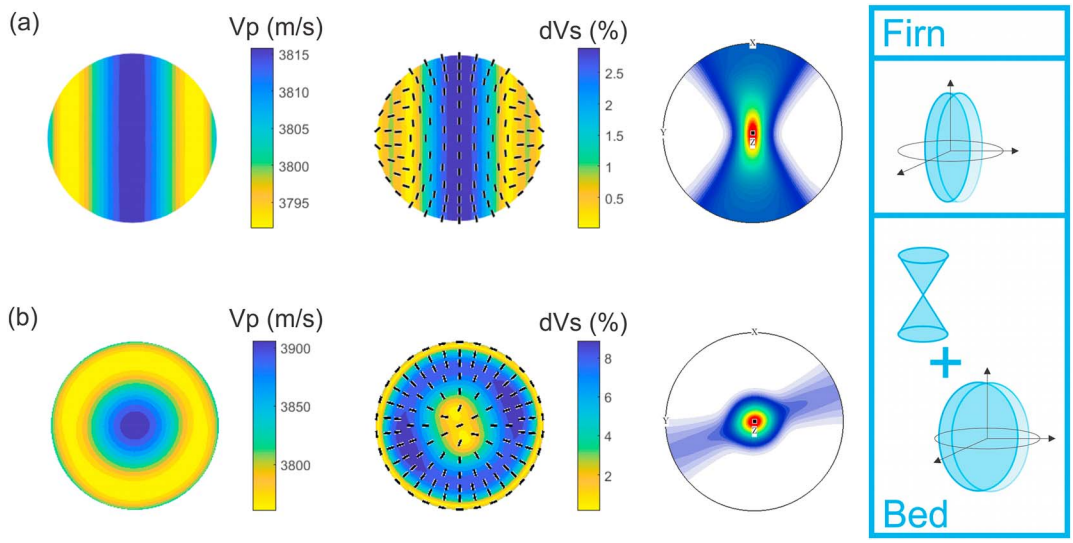

Figure 7. Lower hemisphere plots of *P* wave velocity (V_p), degree of *S* wave splitting (dV_s) with shear wave polarization, and *c* axis density resulting from COF: (a) girdle fabric formed in situ at Korff ice divide and (b) cluster fabric formed at depth at Korff ice divide due to uniaxial compression and lateral extension with overprinting COF resulting from previously strain. (c) Summary of preferred COF model with isotropic firn over two layers of COF as presented in (a) and (b). Results are plotted using the MSAT routine of Walker and Wookey (2012).

third model, the lower girdle component was rotated at 10° intervals through 180° to determine the symmetry axis orientation that minimizes the misfit to the *S* wave splitting measurements.

Shear wave splitting measurements provide the most unambiguous measure of fabric and are compared to the three COF velocity models described (Figure 6 and Table 2). The isotropic model does not display shear wave splitting and cannot therefore describe our observations. Shear wave splitting in the steady state ice divide model is symmetric about the divide axis and exhibits the greatest degree of splitting along the divide axis. This is not in agreement with the observations, where splitting is asymmetric about the divide axis. The rotated-girdle model exhibits more than twice the degree of splitting along the K01 and K02 azimuths than along K03, in agreement with the observations. Although the steady state model improves the mean misfit to the splitting observations compared to the isotropic model (6.7 compared with 30.9 ms), the rotated-girdle model exhibits the lowest mean misfit to the observations of 1.3 ms, and also clearly displays the asymmetry about the divide axis characteristic of the splitting measurements. A suite of fabric orientations and mixing ratios was tested. In the best fit model, the lower girdle fabric is rotated 70° ± 15° east of the ridge axis, or upper girdle fabric (symmetry axis to 023° ± 15° true bearing), to minimize the misfit to shear wave splitting measurements (Figure 7). A mixing ratio of 60% cluster to 40% girdle is required.

6.3. Comparison of Phase-Sensitive Radar and Seismic Fabric Models

To compare the seismic and ApRES results we describe the orientation of the fabric by the eigenvalues of an ellipsoid fit. The difference in the horizontal eigenvalues of a vertical girdle fabric indicates the strength of the fabric, with greater differences indicating a stronger fabric. The elasticity tensor provides the best fit to the seismic observations indicates a difference in the horizontal eigenvalues of 0.38 in the upper layer and 0.20 in the lower layer (Figure 8a).

For the ApRES data, the depth of the quadrant pattern in the phase difference in the lower layer at around 450 m (Figure 4b) can be used to estimate the strength of the fabric in the lower layer. However, there is no quadrant pattern visible in the phase difference in the upper layer, and therefore, the strength of the fabric above the transition at 230 m depth cannot be constrained directly. We therefore test for a range of likely fabric strengths in the upper layer to estimate the range of possible fabric strengths in the lower layer (Figure 8a). For each tested fabric strength in the upper layer we vary the strength in the lower layer to fit the depth of the quadrant pattern in the phase difference. As the ApRES measurements can only

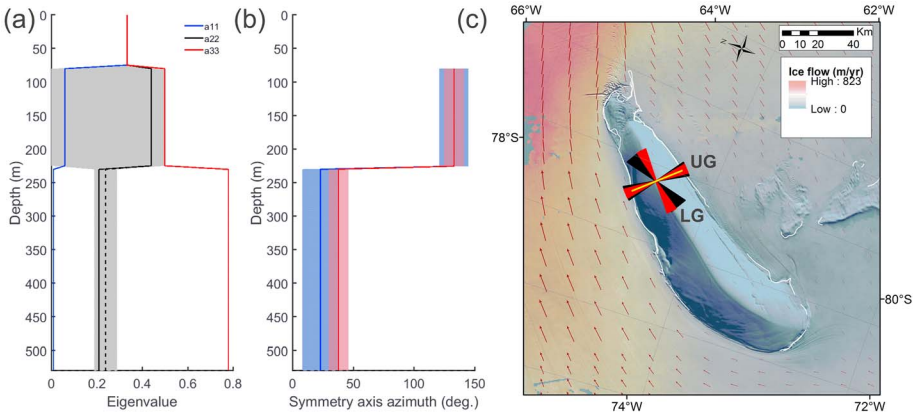

Figure 8. Ice crystal fabric data. (a) Eigenvalues of the fabrics which provide the best fit to the seismic observations. The gray shading indicates the range of fabrics which satisfy the ApRES observations assuming a range of shallow fabric strengths. The black dashed line represents the lower fabric which satisfies the ApRES observations assuming the upper fabric which best fits the seismic observations. (b) Azimuth of the girdle symmetry axis—seismic (blue) and ApRES (red) with uncertainties. (c) Ice flow direction at the northern end of KIR inferred from the orientation of the upper (UG) and lower (LG) girdle fabric symmetry axes. Satellite-derived ice flow velocities with flow-direction vectors (red arrows) and the grounding line (white; Rignot et al., 2011b) are overlain on the MODIS imagery (Scambos et al., 2007). The yellow bar represents present-day ice-divide flow (or girdle symmetry axis) to 133° due to a lateral component of tension, resulting in the shallow girdle fabric. The triangles represent the uncertainty envelope of the best fit of the upper (UG) and lower (LG) girdle fabric symmetry axis envelopes from seismic (black; 133° ± 10° and 023° ± 10°) and radar (red; 133° ± 8° and 038° ± 8°). The lower girdle fabric is consistent with a past ice flow direction parallel to the present-day ice flow of the surrounding shelf.

discriminate the strength of fabric, that is, the difference in horizontal eigenvalues, we fix the smallest horizontal eigenvalue to match that determined by the seismic method. Assuming that the second eigenvalue in the upper layer varies from 0 to 0.5, in order to reproduce the 450-m depth quadrant pattern the second eigenvalue in the lower layer must lie between 0.18 and 0.28. These values are consistent with the fabric strength determined by the seismic observations (Figure 8a). If we fix the strength of the fabric in the upper layer of the ApRES model according to the seismic results, the fabric in the lower layer required to produce a quadrant pattern in ApRES phase difference at 450 m has a horizontal eigenvalue difference of 0.23 compared to 0.20 as determined by the seismic model (Figure 8a). The orientations of the upper and lower girdle fabrics observed by both methods are consistent within uncertainties (Figures 8b and 8c). For clarity, the girdle symmetry-axis orientations from both methods are presented in Figure 8c. Figure 9 presents the synthetic ApRES signal assuming the fabric defined by the best fit seismic results. We see a clear consistency between the observed (Figure 4a) and modeled (Figure 9a) power anomaly. Although the modeled near-surface phase anomaly (Figure 9b) does not match the observations

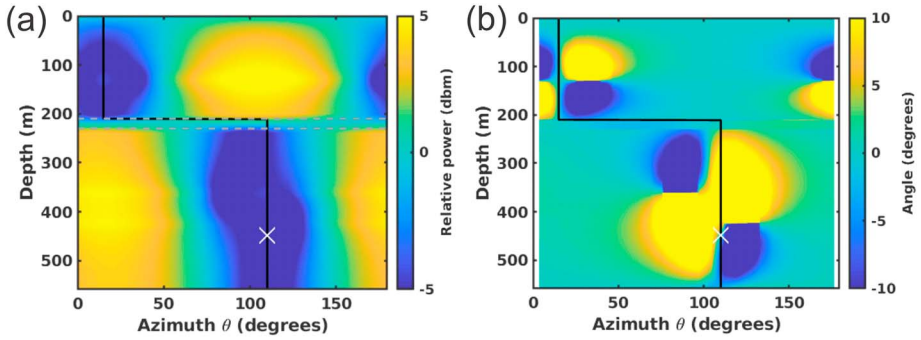

Figure 9. Modeled ApRES response as presented in Figure 4 using the best fit fabric model determined from seismic observations (Figure 7): (a) modeled ApRES power anomaly and (b) modeled ApRES phase difference. The white cross represents the center of the quadrant pattern as observed in the ApRES data (Figure 4).

(Figure 4b), the quadrant pattern in the lower layer resembles the quadrant pattern in the observations. The difference in height within the ice column is a result of inconsistency in the strength of fabric as inferred by the two methods.

The best fit models presented here are the result of the exploration of a parameter space assuming a combination of cluster and girdle fabrics. We assign a girdle fabric to the upper ice layer to match azimuthal variation in both radar and seismic observations. In the same way we can assign a rotated girdle fabric in the lower ice layer. Again, to satisfy the shear wave splitting observations, a cluster fabric is also inferred in the lower ice layer. The best fit models presented here represent the simplest combination of fabrics which satisfy the observations and present the lowest misfit between the tested models and observed measurements. More complex models could undoubtedly be prescribed to satisfy the observations. However, more complex models require more assumptions to be made and render any interpretation less robust.

Using ApRES observations the orientation of the girdle is constrained by measuring the orientation of the maxima and minima in power with depth. An uncertainty of $\pm 8°$ is therefore assigned, determined by the acquisition geometry. The orientation of the girdle constrained by the seismic analysis is determined by minimizing the misfit between the synthetics and observations and results in an uncertainty of $\pm 10°$. Uncertainties in fabric strength are difficult to constrain and quantify for either method as small changes to the fabric geometry affect estimates of fabric strength. As our interpretations are not reliant on our measurements of fabric strength we do not explore the uncertainties in fabric strength any further.

7. Discussion

At an ice divide, where the stress regime is characterized by vertical uniaxial compression with a component of lateral extension, given sufficient time a fabric consisting of a shallow vertical girdle overlying a vertical cluster will develop (Martin et al., 2009). However, at KIR, azimuthal variation in radar backscatter power anomaly and phase difference, as well as asymmetry in seismic velocities and shear wave splitting observations, indicates a more complex fabric. A distinct transition in fabric is observed at 200–230-m depth. The fabric in the upper layer can be described by a vertical girdle fabric. The upper fabric symmetry axis orientation is coincident with the current direction of ice flow at the site (134° true bearing), and perpendicular to the ridge axis. This observation indicates that if the fabric producing anisotropic scattering is flow-induced it is reasonable to assume that both the direction of extension and the direction of variations in fabric are related. The fabric in the lower layer can be described by a cluster fabric combined with a vertical girdle fabric with the symmetry axis rotated approximately perpendicular to the present-day shallow girdle fabric. The girdle fabric in the upper layer and the cluster component of the fabric in the lower layer is likely a reflection of the present-day ice divide flow (Martin et al., 2009). This characteristic ice-divide fabric appears to be in the process of overprinting a remnant exotic fabric within the lower part of the ice column.

The seismic observations presented here measure travel time difference or birefringence from the bulk fabric, integrating the effects along the raypath. The ApRES observations however delineate both anisotropic scattering and birefringence. Anisotropic scattering results from changes in fabric with depth through the ice column. Birefringence, as per the seismic measurements, results from bulk properties integrated over the raypath. Despite the contrast in mechanisms, both scattering and birefringence are undoubtedly caused by preferential alignment of ice crystals as a result of strain. At KIR, both radar and seismic observations indicate the presence of two distinct vertical girdle fabrics in the ice column, consistently indicating divide flow-induced fabric with an additional rotated fabric at depth.

The time taken to overprint a preexisting fabric is dependent on temperature, strain rate, and stress regime and is in general poorly constrained. However, it is generally accepted that following a change in stress regime, in the absence of recrystallization low strain rates, will take significant time to eradicate preexisting fabric. Therefore, a complex strain history leads to a complex fabric (Alley, 1988). Outside of the laboratory, the details of the processes involved in fabric formation and eradication are still poorly constrained. Therefore, with this degree of uncertainty, we make the assumption that a measured COF distribution that does not reflect the current ice flow regime is a remnant of past ice flow.

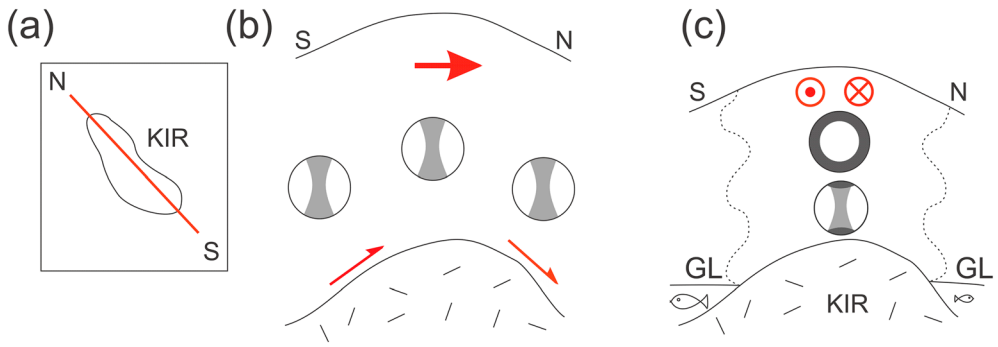

Figure 10. Two-stage schematic side elevation of the evolutionary stages of COF as measured at KIR. (a) Sketch map outlining the location of the following schematic cross sections across KIR. (b) In order that the rotated girdle fabric established upstream (light gray) reaches KIR ice must have advected in a northerly direction across KIR as thicker grounded ice around the LGM. Ice flow direction is in red. (c) Post-LGM retreat and thinning resulted in ice dynamic change eventually stabilizing at the current ice divide position. Ice divide fabric (dark gray) then overprints the preexisting rotated girdle fabric. The gray shading darkens from oldest to youngest, development represented by Schmidt plots of *c* axis distribution. Between stages (b) and (c), either monotonic retreat or retreat followed by readvance is viable but thinning to the point of ungrounding is regarded as unlikely as this would have produced englacial features not observed at KIR.

Kingslake et al. (2016) acquired ice-penetrating radar profiles across our field site and at a location further south on KIR, where they undertook Raymond Effect Dating, which utilizes the distinctive englacial structure of ice divides that results from nonlinear ice-flow behavior, to constrain flow history. Comparison of radargrams from each location shows that the age of the isochron that coincides with the transition in fabric at 230-m depth at north KIR corresponds, within the uncertainties of the Raymond Effect Dating method, to the onset time of ice divide flow at KIR (1.8–2.9 ka B.P.). The transition between contrasting ice fabrics observed here is therefore coincident with the snow surface at the onset of present-day divide flow. The fabric below this depth is different to that expected with ice divide flow and therefore indicates that the preceding flow regime was manifestly different to the current flow. The nature of this preceding flow regime has previously not been constrained. Kingslake et al. (2016) demonstrated that KIR is not in steady state and infer that ice-divide flow began in its present orientation and location around 2.5 ka B.P. Due to the conditions at KIR during ice divide flow, including low strain rates and low temperatures, we assign the lower girdle fabric to this previous strain episode. This preexisting girdle fabric at depth is consistent with two possible previous flow regimes, either (1) an ice divide orientated with its axis approximately perpendicular to the present-day configuration or (2) ice flow in an approximately north-south direction prior to ice divide formation. As we are unable to distinguish either flow regime from the fabric alone, we now discuss the likelihood of each model in relation to other observations.

At KIR the bed geometry broadly precludes a rotated ice divide in the current location as divide stability relies on favorable bed topography; the north-south trending ridge geometry of the bed at KIR is unlikely to support an ice divide with an east-west oriented divide axis. We therefore argue that the remnant fabric results from ice advected northward from Institute Ice Stream and overriding KIR, with a flow direction similar to that observed today around the margins of KIR (Figure 8c). By definition, the current ice divide configuration precludes ice from upstream being advected on to KIR. Therefore, prior to the current episode of divide flow, ice flow must have been distinct from that occurring today, with flow over the current location of KIR either ungrounded as an ice shelf, weakly grounded as an ice rumple, or grounded and sliding over a warm bed. Flow-induced anisotropy in any of these scenarios will be dominated by extension in the direction of flow, resulting in a vertical girdle with symmetry axis perpendicular to the direction of flow, the extent of which will be controlled by the fraction of basal shear. As such, the relic fabric at KIR is consistent with all of these models whereby ice from upstream with an exotic fabric is advected over KIR (Figure 10b).

Two scenarios have been proposed for the retreat of the grounding line from its maximum extent at around 20 ka B.P: (1) monotonic retreat to the present-day configuration (e.g., Hillenbrand et al., 2014; Siegert et al.,

2013) or (2) a rapid retreat to behind the present-day position followed by readvance due to either ice rise capture or grounding line stabilization following GIA (Bradley et al., 2015; Kingslake et al., 2018; Siegert et al., 2013). Both models indicate enhanced flow of a thicker ice sheet over KIR prior to and during initial grounding line retreat (Figure 10b). However, a grounding line behind the present-day configuration indicates a thinner ice shelf than at present over KIR, and as a consequence, further and possibly full ungrounding at the present-day ice rise. Due to the absence of internal or basal deformation features associated with regrounding, Kingslake et al. (2016) inferred slow flow in this location immediately prior to the onset of the current flow regime. This scenario is consistent with reconstructions of the Holocene ice sheet configuration in the Weddell Sea by Hillenbrand et al. (2014), which invoke monotonic retreat and indicate a grounding line in advance of the present-day position at 5–10 ka B.P., with grounded ice overriding KIR at that stage. Continued retreat and stagnation would have initiated the switch from streaming to ice divide flow at KIR, consistent with the observations of fabric presented here. Similarly, at Bungenstock Ice Rise (BIR) disrupted deep radar layering and remnant ice flow lineations at the surface are consistent with enhanced flow as recently as the mid-Holocene, becoming stagnant in the late Holocene, with the Institute and Möller Ice Streams switching to become tributaries of the Ronne Ice Shelf rather than the Filchner Ice Shelf (Siegert et al., 2013). Intensely buckled and discontinuous layering in tributaries to Institute Ice Stream (Winter et al., 2015) indicates that enhanced flow previously took ice over BIR but switched to the current flow orientation with cessation of enhanced flow over BIR.

The ice sheet reconstructions of Bradley et al. (2015) and Kingslake et al. (2018) indicate grounding line retreat behind the present-day position to a minimum ice sheet extent at some time during the Holocene, followed by readvance to the current position. Siegert et al. (2013) also offer a second scenario to explain disrupted layering at BIR which requires post-LGM GIA and readvance. Readvance of the grounding line to its current position implies a reversal of post-LGM retreat while the ice streams were grounded on reverse-bed slopes. Although these authors invoke GIA as a likely cause of retreat stabilization, Gudmundsson (2013) demonstrated that ice-shelf buttressing can also stabilize otherwise unstable grounding line positions. These ice sheet reconstructions indicate near-ungrounding or possible complete ungrounding at KIR. In this scenario, during readvance ice from upstream is advected over KIR as a floating ice shelf or partially grounded ice rumples, bringing ice with a preexisting fabric on to KIR prior to ice divide formation. During readvance and thickening, transition from ice shelf to ice rise would likely have resulted in crevassing, as observed at HIR. The absence of buried crevasses or disrupted layering at depth at KIR (Kingslake et al., 2016) may indicate that this site was grounded prior to flow reorganization at 2.5 ka. Kingslake et al. (2018) hypothesize that these features may have subsequently advected away or been buried and thinned to such a degree that they are no longer visible in the radar sections, thus not precluding a period of near-complete ungrounding or regrounding.

Although neither KIR nor HIR exhibit relict flow stripes as observed at BIR, buried relic crevasses and disrupted layers at depth at HIR are consistent with fast flow prior to the present-day slow divide flow as currently observed at the Doake Ice Rumples (Kingslake et al., 2018). As stated, there is no evidence of buckled layers at depth at KIR (Kingslake et al., 2016). However, the shallowest bed below HIR is lower than beneath KIR by around 100 m and therefore during retreat HIR would unground more readily than KIR. Alternatively, due to this contrast in bed elevation, during readvance KIR may have regrounded earlier than HIR, providing sufficient time for englacial evidence of this event to advect over the grounding line. A transition through a phase of ice rumples at KIR during the period of regrounding would allow advection of ice from upstream prior to divide formation. However, reconciling the relative timing of the initiation of ice divide flow at KIR and HIR remains an open question.

The contrast in englacial structure at Korff and Henry Ice Rises highlights that these ice rises are potentially highly diagnostic sites for constraining ice sheet history where other direct measurements such as exposure age dating are unavailable. It is possible that KIR has remained grounded while HIR ungrounded. This difference in behavior provides two distinct data points in close proximity which need to be validated contemporaneously in models which invoke GIA to control ice sheet retreat and readvance. Although the measurements presented here are insufficient to constrain unambiguously the recent flow history of the Weddell Sea region it is clear that englacial structure and fabric of ice rises are key diagnostics for constraining recent ice flow. Further measurements of fabric at other key sites such as the Korff, Henry, and

Bungenstock Ice Rises, complementing radar observations that reveal englacial structure and deformation, would help further constrain ice sheet history by characterizing any previous flow regimes which remain imprinted in the fabric of the ice column.

Although the data presented here have allowed discrimination of fabric at KIR, improvements could be made in future field campaigns to enhance the analytical capabilities of the data acquired. A strength of the ApRES method lies in the speed with which measurements can be made. The seismic technique, despite significantly more involved acquisition, complements the ApRES measurements and can be used to distinguish forms of anisotropy which are azimuthally symmetric, such as the vertical cluster, and also determine the strength of fabric with less ambiguity than the ApRES method. By using both methods in parallel the fabric can be derived with less ambiguity than using either method in isolation. Although these data have allowed us to determine the COF, improvements could be made to the seismic acquisition in future programs. For example, three-component sensors would reduce uncertainty in the shear wave splitting calculations. This would be best achieved with standalone sensors with sufficient clock accuracy to mitigate the need for cable-based systems. Without a priori knowledge of the fabric it is impossible to determine the shot hole depth which would preclude coincident arrivals of the surface ghost and, for example, slow shear wave arrivals. Therefore, use of at least two shot depths would allow direct discrimination. A surface source of sufficient magnitude to produce reliable *P* and *S* wave energy would remove the ghost entirely. Likewise, a shear wave source of known geometry would remove ambiguity in fabric inversion. Due to the complexity of the anisotropic system and range of fabrics likely in ice, the next step would be to implement an inversion of seismic travel times and polarizations rather than testing a suite of viable fabric combinations as has been carried out in this study, and eventually a full waveform inversion methodology on the seismic data.

8. Conclusions

For the first time, the analysis of polarimetric phase-sensitive radar data and seismic data has been reconciled to constrain fabric within the ice column. Modeling of ApRES measurements indicates two orthogonal girdle fabrics within the ice column, with a transition at 200–230-m depth between the two orientations. ApRES return power anomalies indicate a girdle fabric at shallow depth consistent with ice divide flow. At greater depth, a quadrant pattern in the return phase difference indicates a second girdle fabric, orthogonal to the upper girdle. Due to the nature of the measurements, azimuthally invariant fabric cannot be constrained by ApRES, but can be characterized using seismic measurements. Within uncertainties, seismic observations are in agreement with the ApRES results. An upper girdle fabric is delineated using diving *P* and *S* wave velocities from raypaths at the top of the ice column. The base of this layer is assigned to 200 m by a transition in fabric observed in the polarimetric ApRES measurements. Below 230-m depth a vertical cluster fabric with a concomitant vertical girdle fabric rotated $70 \pm 15°$ east provides the best fit to the shear wave splitting observations. This degree of splitting cannot be achieved without a component of cluster fabric at depth, consistent with the ongoing development of fabric at depth at ice divides due to vertical compression and lateral flow away from the linear divide. The nature of the fabric determined independently by both methods is consistent despite sensitivity to different physical properties.

These measurements have allowed us to delimit the current and residual COF, demonstrating that the fabric induced by the present-day ice divide configuration is overprinting a preexisting fabric. As a result, the recent ice flow history at KIR has been further constrained, providing additional data on ice flow history in the Weddell Sea area, where measurements are otherwise sparse. A rotated girdle fabric at depth is consistent with a previous episode of rotated ice divide or streaming flow. Due to the absence of englacial features associated with grounding, our favored interpretation is streaming flow from Institute Ice Stream in the south, overriding KIR without ungrounding, prior to ice divide formation.

Although the data presented here provide constraints on the fabric and flow history around KIR, further measurements along the length of KIR may help delimit the extent of flow change in relation to bed geometry. We also advocate for further measurements across all ice divides of the Weddell Sea area to constrain more fully the regional flow history. The glacial history of the West Antarctic Ice Sheet could be further constrained by additional measurements across the Ross Sea area where a similar history of flow switching and stagnation has been reported (Conway et al., 1999), forming two discrete yet linked components of the deglaciation of West Antarctica (Kingslake et al., 2018).

Acknowledgments

This study is part of the British Antarctic Survey program Polar Science for Planet Earth. All data were collected with the support of the British Antarctic Survey. The ApRES fieldwork were funded by Natural Environmental Research Council grant NE/J008087/1, led by Richard Hindmarsh. Thanks to Scott Webster for the assistance in the field. We thank Bryn Hubbard, the Editor, Anja Diez, and another anonymous reviewer for their comments and suggestions that have improved this paper. Data are available through NERC's Polar Data Centre: https://doi.org/10/cvxn and https://doi.org/10/cvxq.

References

Alley, R. B. (1988). Fabrics in polar ice sheets: development and prediction. *Science*, *240*(4851), 493–495.

Azuma, N. (1994). A flow law for anisotropic ice and its application to ice sheets. *Earth and Planetary Science Letters*, *128*(3–4), 601–614. https://doi.org/10.1016/0012-821x(94)90173-2

Azuma, N., & Higashi, A. (1985). Formation processes of ice fabric pattern in ice sheets. *Annals of Glaciology*, *6*, 130–134. https://doi.org/10.3189/1985AoG6-1-130-134

Azuma, N., Wang, Y., Mori, K., Narita, H., Hondoh, T., Shoji, H., & Watanabe, O. (1999). Textures and fabrics in the dome F (Antarctica) ice core. In T. H. Jacka (Ed.), *Annals of Glaciology* (Vol. 29, pp. 163–168).

Baan, M. v. d., & Kendall, J. M. (2002). Estimating anisotropy parameters and traveltimes in the τ-p domain. *Geophysics*, *67*(4), 1076–1086. https://doi.org/10.1190/1.1500368

Bargmann, S., Seddik, H., & Greve, R. (2012). Computational modeling of flow-induced anisotropy of polar ice for the EDML deep drilling site, Antarctica: The effect of rotation recrystallization and grain boundary migration. *International Journal for Numerical and Analytical Methods in Geomechanics*, *36*(7), 892–917. https://doi.org/10.1002/nag.1034

Bentley, M. J. (1999). Volume of Antarctic ice at the last glacial maximum, and its impact on global sea level change. *Quaternary Science Reviews*, *18*(14), 1569–1595. https://doi.org/10.1016/S0277-3791(98)00118-8

Bentley, M. J., Fogwill, C. J., Le Brocq, A. M., Hubbard, A. L., Sugden, D. E., Dunai, T. J., & Freeman, S. P. H. T. (2010). Deglacial history of the West Antarctic ice sheet in the Weddell Sea embayment: Constraints on past ice volume change. *Geology*, *38*(5), 411–414. https://doi.org/10.1130/g30754.1

Bingham, R. G., Rippin, D. M., Karlsson, N. B., Corr, H. F. J., Ferraccioli, F., Jordan, T. A., et al. (2015). Ice-flow structure and ice dynamic changes in the Weddell Sea sector of West Antarctica from radar-imaged internal layering. *Journal of Geophysical Research: Earth Surface*, *120*, 655–670. https://doi.org/10.1002/2014jf003291

Bradley, S. L., Hindmarsh, R. C. A., Whitehouse, P. L., Bentley, M. J., & King, M. A. (2015). Low post-glacial rebound rates in the Weddell Sea due to Late Holocene ice-sheet readvance. *Earth and Planetary Science Letters*, *413*, 79–89. https://doi.org/10.1016/j.epsl.2014.12.039

Clark, P. U., Dyke, A. S., Shakun, J. D., Carlson, A. E., Clark, J., Wohlfarth, B., Mitrovica, J. X., et al. (2009). The last glacial maximum. *Science*, *325*(5941), 710–714. https://doi.org/10.1126/science.1172873

Conway, H., Hall, B. L., Denton, G. H., Gades, A. M., & Waddington, E. D. (1999). Past and future grounding-line retreat of the West Antarctic ice sheet. *Science*, *286*(5438), 280–283. https://doi.org/10.1126/science.286.5438.280

DeConto, R. M., & Pollard, D. (2016). Contribution of Antarctica to past and future sea-level rise. *Nature*, *531*, 591–597. https://doi.org/10.1038/nature17145

Diez, A., Bromirski, P. D., Gerstoft, P., Stephen, R. A., Anthony, R. E., Aster, R. C., et al. (2016). Ice shelf structure derived from dispersion curve analysis of ambient seismic noise, Ross ice shelf, Antarctica. *Geophysical Journal International*, *205*(2), 785–795. https://doi.org/10.1093/gji/ggw036

Diez, A., & Eisen, O. (2015). Seismic wave propagation in anisotropic ice—Part 1: Elasticity tensor and derived quantities from ice-core properties. *The Cryosphere*, *9*(1), 367–384. https://doi.org/10.5194/tc-9-367-2015

Diez, A., Eisen, O., Hofstede, C., Lambrecht, A., Mayer, C., Miller, H., et al. (2015). Seismic wave propagation in anisotropic ice—Part 2: Effects of crystal anisotropy in geophysical data. *The Cryosphere*, *9*(1), 385–398. https://doi.org/10.5194/tc-9-385-2015

Diprinzio, C. L., Wilen, L. A., Alley, R. B., Fitzpatrick, J. J., Spencer, M. K., & Gow, A. J. (2005). Fabric and texture at Siple dome, Antarctica. *Journal of Glaciology*, *51*(173), 281–290. https://doi.org/10.3189/172756505781829359

Drews, R., Eisen, O., Steinhage, D., Weikusat, I., Kipfstuhl, S., & Wilhelms, F. (2012). Potential mechanisms for anisotropy in ice-penetrating radar data. *Journal of Glaciology*, *58*(209), 613–624. https://doi.org/10.3189/2012JoG11J114

Durand, G., Gillet-Chaulet, F., Svensson, A., Gagliardini, O., Kipfstuhl, S., Meyssonnier, J., Parrenin, F., et al. (2007). Change in ice rheology during climate variations—Implications for ice flow modelling and dating of the EPICA dome C core. *Climate of the Past*, *3*(1), 155–167. https://doi.org/10.5194/cp-3-155-2007

Duval, P., Ashby, M., & Anderman, I. (1983). Rate-controlling processes in the creep of polycrystalline ice. *The Journal of Physical Chemistry*, *87*(21), 4066–4074. https://doi.org/10.1021/j100244a014

Eisen, O., Hamann, I., Kipfstuhl, S., Steinhage, D., & Wilhelms, F. (2007). Direct evidence for continuous radar reflector originating from changes in crystal-orientation fabric. *The Cryosphere*, *1*(1), 1–10.

Faria, S. H., Weikusat, I., & Azuma, N. (2014). The microstructure of polar ice. Part II: State of the art. *Journal of Structural Geology*, *61*, 21–49. https://doi.org/10.1016/j.jsg.2013.11.003

Fujita, S., Maeno, H., & Matsuoka, K. (2006). Radio-wave depolarization and scattering within ice sheets: a matrix-based model to link radar and ice-core measurements and its application. *Journal of Glaciology*, *52*(178), 407–424. https://doi.org/10.3189/172756506781828548

Gudmundsson, G. H. (2013). Ice-shelf buttressing and the stability of marine ice sheets. *The Cryosphere*, *7*(2), 647–655. https://doi.org/10.5194/tc-7-647-2013

Guest, W. S., & Kendall, J. M. (1993). Modelling seismic waveforms in anisotropic inhomogeneous media using ray and Maslov asymptotic theory: Application to exploration seismology. *Canadian Journal of Exploration Geophysics*, *29*(1), 78–92.

Gusmeroli, A., Pettit, E. C., Kennedy, J. H., & Ritz, C. (2012). The crystal fabric of ice from full-waveform borehole sonic logging. *Journal of Geophysical Research*, *117*, F03021. https://doi.org/10.1029/2012JF002343

Hargreaves, N. D. (1977). The polarization of radio signals in the radio echo sounding of ice sheets. *Journal of Physics D: Applied Physics*, *10*(9), 1285–1304. https://doi.org/10.1088/0022-3727/10/9/012

Hill, R. (1952). The elastic behaviour of a crystalline aggregate. *Proceedings of the Physical Society. Section A*, *65*(5), 349–354. https://doi.org/10.1088/0370-1298/65/5/307

Hillenbrand, C. D., Bentley, M. J., Stolldorf, T. D., Hein, A. S., Kuhn, G., Graham, A. G. C., et al. (2014). Reconstruction of changes in the Weddell Sea sector of the Antarctic ice sheet since the last glacial maximum. *Quaternary Science Reviews*, *100*, 111–136. https://doi.org/10.1016/j.quascirev.2013.07.020

King, E. C., & Jarvis, E. P. (2007). Use of shear waves to measure Poisson's ratio in polar firn. *Journal of Environmental and Engineering Geophysics*, *12*(1), 15–21. https://doi.org/10.2113/JEEG12.1.15

Kingslake, J., Martin, C., Arthern, R. J., Corr, H. F. J., & King, E. C. (2016). Ice-flow reorganization in West Antarctica 2.5 kyr ago dated using radar-derived englacial flow velocities. *Geophysical Research Letters*, *43*, 9103–9112. https://doi.org/10.1002/2016gl070278

Kingslake, J., Scherer, R., Albrecht, T., Coenen, J., Powell, R., Reese, R., et al. (2018). Extensive Holocene West Antarctic ice sheet retreat and rebound driven re-advance. *Nature*, *558*, 430–434. https://doi.org/10.1038/s41586-018-0208-x

Kirchner, J. F., & Bentley, C. R. (1990). RIGGS III: Seismic short-refraction studies using an analytical curve-fitting technique. *Antarctic Research Series*, *42*, 109–126.

Lipenkov, V. Y., Barkov, N. I., Duval, P., & Pimienta, P. (1989). Crystalline texture of the 2083-M ice Core at Vostok Station, Antarctica. *Journal of Glaciology*, *35*(121), 392–398. https://doi.org/10.1017/S0022143000009321

Martin, C., Gudmundsson, G. H., Pritchard, H. D., & Gagliardini, O. (2009). On the effects of anisotropic rheology on ice flow, internal structure, and the age-depth relationship at ice divides. *Journal of Geophysical Research*, *114*, F04001. https://doi.org/10.1029/2008JF001204

Matsuoka, K., Furukawa, T., Fujita, S., Maeno, H., Uratsuka, S., Naruse, R., & Watanabe, O. (2003). Crystal orientation fabrics within the Antarctic ice sheet revealed by a multipolarization plane and dual-frequency radar survey. *Journal of Geophysical Research*, *108*, 2499. https://doi.org/10.1029/2003JB002425

Matsuoka, K., Wilen, L., Hurley, S. P., & Raymond, C. F. (2009). Effects of birefringence within ice sheets on obliquely propagating radio waves. *IEEE Transactions on Geoscience and Remote Sensing*, *47*(5), 1429–1443. https://doi.org/10.1109/tgrs.2008.2005201

Maurel, A., Lund, F., & Montagnat, M. (2015). Propagation of elastic waves through textured polycrystals: Application to ice. *Proceedings of the Royal Society a-Mathematical Physical and Engineering Sciences, 471*(2177), 20140988. https://doi.org/10.1098/rspa.2014.0988

Montagnat, M., Buiron, D., Arnaud, L., Broquet, A., Schlitz, P., Jacob, R., & Kipfstuhl, S. (2012). Measurements and numerical simulation of fabric evolution along the tabs dome ice core, Antarctica. *Earth and Planetary Science Letters*, *357-358*, 168–178. https://doi.org/10.1016/j.epsl.2012.09.025

Mulvaney, R., Alemany, O., & Possenti, P. (2007). The Berkner Island (Antarctica) ice-core drilling project. *Annals of Glaciology*, *47*, 115–124. https://doi.org/10.3189/172756407786857758

Nicholls, K. W., Corr, H. F. J., Stewart, C. L., Lok, L. B., Brennan, P. V., & Vaughan, D. G. (2015). A ground-based radar for measuring vertical strain rates and time-varying basal melt rates in ice sheets and shelves. *Journal of Glaciology*, *61*(230), 1079–1087. https://doi.org/10.3189/2015JoG15J073

Picotti, S., Vuan, A., Carcione, J. M., Horgan, H. J., & Anandakrishnan, S. (2015). Anisotropy and crystalline fabric of Whillans ice stream (West Antarctica) inferred from multicomponent seismic data. *Journal of Geophysical Research: Solid Earth*, *120*, 4237–4262. https://doi.org/10.1002/2014JB011591

Raymond, C. F. (1983). Deformation in the vicinity of ice divides. *Journal of Glaciology*, *29*(103), 357–373. https://doi.org/10.1017/S0022143000030288

Rignot, E., Mouginot, J., & Scheuchl, B. (2011a). Ice flow of the Antarctic ice sheet. *Science*, *333*, 1427–1430. https://doi.org/10.1126/science.1208336

Rignot, E., Mouginot, J., & Scheuchl, B. (2011b). Antarctic grounding line mapping from differential satellite radar interferometry. *Geophysical Research Letters*, *38*, L10504. https://doi.org/10.1029/2011GL047109

Ross, N., Bingham, R., Corr, H. F. J., Ferraccioli, F., Jordan, T., Le Brocq, A., et al. (2012). Steep reverse bed slope at the grounding line of the Weddell Sea sector in West Antarctica. *Nature Geoscience*, *5*(6), 393–396. https://doi.org/10.1038/ngeo1468

Savage, M. K. (1999). Seismic anisotropy and mantle deformation: What have we learned from shear wave splitting? *Reviews of Geophysics*, *37*(1), 65–106. https://doi.org/10.1029/98RG02075

Scambos, T. A., Haran, T. M., Fahnestock, M. A., Painter, T. H., & Bohlander, J. (2007). MODIS-based mosaic of Antarctica (MOA) data sets: Continent-wide surface morphology and snow grain size. *Remote Sensing of Environment*, *111*(2–3), 242–257. https://doi.org/10.1016/j.rse.2006.12.020

Siegert, M., Ross, N., Corr, H., Kingslake, J., & Hindmarsh, R. (2013). Late Holocene ice-flow reconfiguration in the Weddell Sea sector of West Antarctica. *Quaternary Science Reviews*, *78*, 98–107. https://doi.org/10.1016/j.quascirev.2013.08.003

Silver, P. G., & Chan, W. W. (1991). Shear wave splitting and subcontinental mantle deformation. *Journal of Geophysical Research*, *96*(B10), 16,429–16,454. https://doi.org/10.1029/91JB00899

Smith, E. C., Baird, A. F., Kendall, J. M., Martín, C., White, R. S., Brisbourne, A. M., & Smith, A. M. (2017). Ice fabric in an Antarctic ice stream interpreted from seismic anisotropy. *Geophysical Research Letters*, *44*, 3710–3718. https://doi.org/10.1002/2016gl072093

Teanby, N. A., Kendall, J. M., & Van der Baan, M. (2004). Automation of shear-wave splitting measurements using cluster analysis. *Bulletin of the Seismological Society of America*, *94*(2), 453–463. https://doi.org/10.1785/0120030123

Thorsteinsson, T., Kipfstuhl, J., & Miller, H. (1997). Textures and fabrics in the GRIP ice core. *Journal of Geophysical Research*, *102*(C12), 26,583–26,599. https://doi.org/10.1029/97JC00161

Velicogna, I., & Wahr, J. (2006). Measurements of time-variable gravity show mass loss in Antarctica. *Science*, *311*(5768), 1754–1756. https://doi.org/10.1126/science.1123785

Walker, A. M., & Wookey, J. (2012). MSAT—A new toolkit for the analysis of elastic and seismic anisotropy. *Computers & Geosciences*, *49*, 81–90. https://doi.org/10.1016/j.cageo.2012.05.031

Wang, Y., Kipfstuhl, S., Azuma, N., Thorsteinsson, T., & Miller, H. (2003). Ice-fabrics study in the upper 1500 m of the dome C (East Antarctica) deep ice core. In P. Duval (Ed.), *Annals of Glaciology* (Vol. 37, pp. 97–104).

Wang, Y., Thorsteinsson, T., Kipfstuhl, J., Miller, H., DahlJensen, D., & Shoji, H. (2002). A vertical girdle fabric in the NorthGRIP deep ice core, North Greenland. In E. W. Wolff (Ed.), *Annals of Glaciology* (Vol. 35, pp. 515–520).

Weikusat, I., Jansen, D., Binder, T., Eichler, J., Faria, S. H., Wilhelms, F., et al. (2017). Physical analysis of an Antarctic ice core—Towards an integration of micro- and macrodynamics of polar ice. *Philosophical Transactions. Series A, Mathematical, Physical, and Engineering Sciences, 375*(2086), 20150347. https://doi.org/10.1098/rsta.2015.0347

Whitehouse, P. L., Bentley, M. J., & Le Brocq, A. M. (2012). A deglacial model for Antarctica: Geological constraints and glaciological modelling as a basis for a new model of Antarctic glacial isostatic adjustment. *Quaternary Science Reviews*, *32*, 1–24. https://doi.org/10.1016/j.quascirev.2011.11.016

Winter, K., Woodward, J., Ross, N., Dunning, S. A., Bingham, R. G., Corr, H. F. J., & Siegert, M. J. (2015). Airborne radar evidence for tributary flow switching in institute ice stream, West Antarctica: Implications for ice sheet configuration and dynamics. *Journal of Geophysical Research: Earth Surface*, *120*, 1611–1625. https://doi.org/10.1002/2015jf003518

York, D., Evensen, N. M., Martínez, M. L., & Delgado, J. D. B. (2004). Unified equations for the slope, intercept, and standard errors of the best straight line. *American Journal of Physics*, *72*(3), 367–375. https://doi.org/10.1119/1.1632486